

Article

Impact of Input Signal Characteristics on Energy-Localization Performance of a Phononic Crystal with a Defect: A Comparative Study of Burst and Continuous Wave Excitation

Soo-Ho Jo 

Department of Mechanical, Robotics, and Energy Engineering, Dongguk University,
Seoul 04620, Republic of Korea; sohojo@dgu.ac.kr; Tel.: +82-2-2260-3702

Abstract: This study examines the energy-localization performance of a one-dimensional phononic crystal (PnC) with a defect when exposed to burst waves of different cycle numbers under longitudinal waves. Using the finite element method, band structures of the defect-introduced PnC were calculated, revealing a phononic band-gap range, defect-band frequencies, and corresponding defect-mode shapes. The transient analysis examined the longitudinal displacement at the center of this defect in the time domain for various burst-wave scenarios. The results indicate that energy-localization performance inside the defect highly depended on the number of cycles. Energy-localization performance was better with larger cycles or continuous waves, although burst waves with a small number of cycles also showed some improvement, albeit limited. Moreover, burst waves with a small number of cycles did not clearly induce fixed-like boundary conditions (in other words, nodal points in standing waves) within the defect-introduced PnC, leading to obscure energy-localized behaviors. Key messages from this work can be summarized as follows. First, comparing the energy-localization performance under incident burst waves with different cycle numbers for different systems might not be appropriate. Second, the physically reasonable formation of defect-mode-enabled energy localization requires burst waves with a large (in the case study, over 500) number of cycles.

Keywords: phononic crystal; phononic band gap; defect mode; energy localization; burst wave



Citation: Jo, S.-H. Impact of Input Signal Characteristics on Energy-Localization Performance of a Phononic Crystal with a Defect: A Comparative Study of Burst and Continuous Wave Excitation. *Crystals* **2023**, *13*, 827. <https://doi.org/10.3390/cryst13050827>

Academic Editor: Luis M. Garcia-Raffi

Received: 25 April 2023

Revised: 14 May 2023

Accepted: 15 May 2023

Published: 16 May 2023



Copyright: © 2023 by the author. Licensee MDPI, Basel, Switzerland. This article is an open access article distributed under the terms and conditions of the Creative Commons Attribution (CC BY) license (<https://creativecommons.org/licenses/by/4.0/>).

1. Introduction

In recent years, there has been a growing interest in research on phononic crystals (PnCs). PnCs are constructed by arranging artificially designed unit cells in a periodic pattern [1–3]. The potential of PnCs to manipulate elastic wave energy has opened up new possibilities for controlling its propagating direction and intensity [4,5]. One promising area of research involves leveraging defects in PnCs to spatially localize elastic waves in specific regions and quantitatively increase their mechanical energy densities (energy per volume). Defect-free PnCs create phononic band gaps in their dispersion relationships, resulting from Bragg scattering [6,7]. However, disordering structures, known as defects, in PnCs generate new passbands, called defect bands. These defect bands have slopes that are close to zero and are located within these band gaps [8,9]. Recently, it has been revealed that—due to the presence of evanescent waves—unit cells that enclose the defect create hypothetical, fixed-end boundary conditions, resulting in a resonating motion near the defect at each frequency of the defect bands [10]. This motion can be referred to as the defect-mode shape [11,12]. These properties allow for the high-density concentration of elastic wave energy inside and near the defect. Inspired by significant energy-localization performance within a narrow frequency range, the potential applications of defect-introduced PnCs have been suggested as narrow bandpass filters [13,14], resonance-type energy harvesters [15,16], sensors [17,18], and actuators [19,20].

Research related to this field largely consists of numerical or analytical modeling to predict the amount of energy localization, new designs to further improve the amount of

energy localization, and experimental demonstration. When examining previous research performed in simulations or experiments, it is important to note that the input signals used in each study can vary significantly. For example, some studies have excited burst waves that consist of only a few or tens of cycles [21–25], while others have excited continuous waves [26–30]. Although the amplitudes (e.g., strain, displacement, or velocity) of these incident waves may be normalized or scaled to be identical, a comparison of the absolute energy-localization performance that can be calculated or measured within the defects across different input signal settings is questionable. Each system has a different number of cycles required to reach a steady state; hence, there are doubts about whether it is fair to compare the performance for specific cycles. Another critical consideration is that phononic band-gap properties result from the destructive interferences that occur due to the continuously repeated generation of reflection and transmission at interfaces where there is a mismatch in impedance between the stacks within the PnCs. Therefore, the generation of defect bands or defect modes can be understood in the same manner as the creation of phononic band gaps. Hence, it is doubtful that burst waves of only a few cycles can consistently produce the physically observable energy localization enabled by defect modes in PnCs, which is similar to the way that resonance-based displacement magnification in vibrations requires a sufficiently continuous supply of mechanical energy.

Motivated by these concerns, the aim of this study was to evaluate the energy-localization performance of a defect-introduced PnC when burst waves with varying numbers of cycles enter the wave-manipulation system. This study considered two reference values for the evaluation of energy localization: the displacement amplitude of incident burst waves and the displacement within the defect obtained from the incident of continuous waves. To achieve this, a parametric study focusing on longitudinal wave propagation was conducted. It can be noted that burst and continuous waves correspond to transient and steady-state analyses, respectively. To enable a quantitative comparison between different cycles and minimize the influence of ambient frequencies, we assumed the use of a sinusoidal burst wave with a single ideal frequency (called the monochromatic wave) instead of general tone-burst waves containing a target frequency and a narrow frequency range near it. Due to the complexity of developing an analytical model of PnCs composed of multiple lattices for transient analysis, this study adopted a numerical approach using the commercial finite-element-based tool COMSOL MULTIPHYSICS 6.1 (developed by COMSOL in Burlington, MA, USA). Observations of this work can be summarized as follows:

- Increasing the number of cycles makes the time to reach the maximum displacement gradually increase and then converge to a certain value;
- Increasing the number of cycles makes the maximum displacement gradually increase and stabilize at the value obtained from time-harmonic analysis;
- For a small number of cycles, the cycle number is dominant when determining the energy-localization performance;
- Energy-localization performance for a small number of burst waves is considerably smaller than the cases of time-harmonic analysis or burst waves with a large number of cycles;

From this perspective, the key messages that this work delivers are as follows:

- Comparing the energy-localization performance under incident burst waves with different cycle numbers for different systems may not be appropriate;
- The physically reasonable formation of defect-mode-enabled energy localization requires burst waves with a large (in this case study, over 500) number of cycles.

The remainder of this paper is structured into several sections. Section 2 describes the system configuration and setup for numerical studies. Section 3 presents and discusses the results of the band structure and transient analyses. Finally, Section 4 provides a summary of the findings and conclusions from this work.

2. System Configuration and Setup for Numerical Studies

Figure 1 visualizes the topic of this study. A one-dimensional PnC is made up of nine-unit cells aligned along the longitudinal axis. Each unit cell comprises two stacks of different materials (gray aluminum and red zinc) attached to each other's cross-section. At the same time, the fifth unit cell contains a defect that is introduced by altering the length of its red stack. All structures share an identical square cross-section with an area of 25 mm^2 . Jo and Youn suggested a specific design for a one-dimensional PnC with a defect to match the defect-band frequency with a target frequency [31]. Following their lead, the lengths of the gray and red stacks were designed to correspond to their respective quarter-wavelengths of 25.82 mm and 16.71 mm at the target frequency of 50 kHz . Similarly, the length of the gray defect was set to match its half-wavelength of 51.64 mm . The mass densities of aluminum and zinc were set as 2700 kg/m^3 and 8500 kg/m^3 , respectively. Young's moduli of aluminum and zinc were set to 72 GPa and 95 GPa , respectively. This PnC itself was used in the band-structure analysis. Additionally, in transient analysis, a semi-infinitely lengthy gray structure (made of aluminum) was bonded on each side of the defect-introduced PnC to create an engineering scenario where incident waves entering toward the front were partially reflected at the front and partially transmitted at the rear.

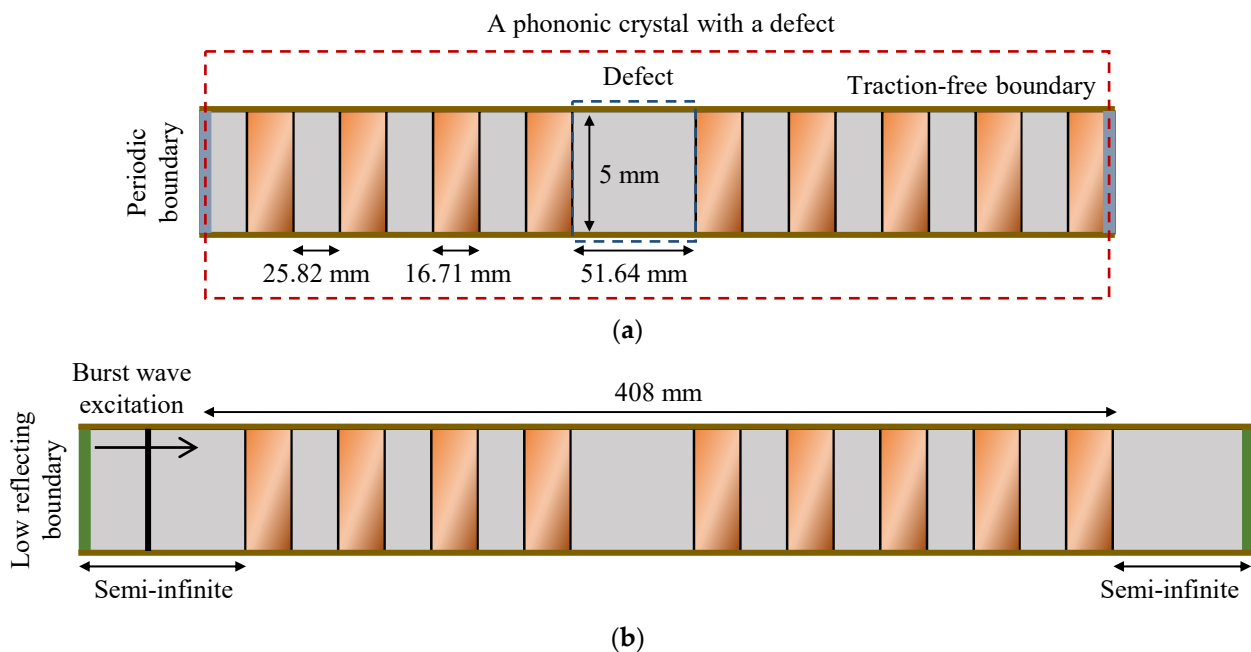


Figure 1. A front view of a target wave-propagation system with a defect-introduced PnC: (a) The structures and numerical setting used in band-structure analysis and (b) The structure and numerical setting used in transient analysis.

Figure 1a shows the configuration of the defect introduced by PnC to analyze its band structures. Figure 2 displays the workflow diagram used in COMSOL to perform the dispersion analysis. The 'Solid Mechanics Physics' and 'Eigenfrequency Study' features were used. First, a two-dimensional spatial domain was defined, and the defect introduced by PnC was constructed using the 'Rectangular' function in the 'Geometry' section. When attaching each interface of the different materials, the continuity conditions of displacement and stress were automatically reflected. At the same time, all surfaces of the defect-introduced PnC were automatically set to be exposed in a traction-free and plane-stress condition. In the 'Physics' section, the 'Floquet Periodicity' setting was applied to both ends of the defect introduced by PnC. To ensure proper meshing, the maximum mesh size was set to 2.5 mm using the 'Mapping' function in the 'Mesh' section after the convergence test shown in Figure 3; Figure 3a,b shows that the peak frequency and corresponding displacement in the time-harmonic analysis converged to their specific values when the

mesh size became less than 3 mm and 2.5 mm, respectively. By sweeping the real-valued Bloch wavenumber over the Brillouin zone in the ‘Floquet Periodicity’ setting, the final band structures were obtained. Under longitudinal waves, the range of the phononic band gap was the region where two eigenfrequencies are obtained at either end of the Brillouin zone. The defect bands were the narrow complex-valued (non-zero real part) eigenfrequency ranges that corresponded to a set of Bloch wavenumbers inside the Brillouin zone within the calculated phononic band gap. Additionally, the displacement field (eigenvectors) at each defect-band frequency represented the defect-mode shape, providing a visualization of how elastic wave energy was concentrated.

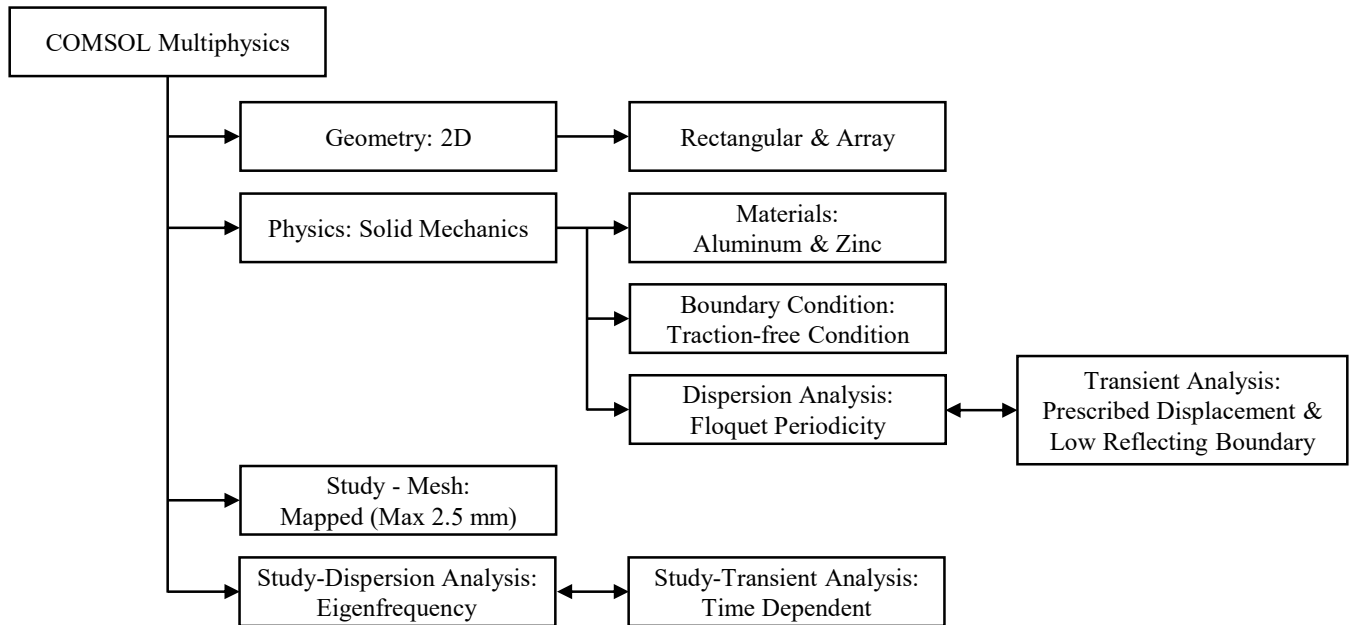


Figure 2. The workflow diagram in COMSOL Multiphysics to perform dispersion or transient analyses.

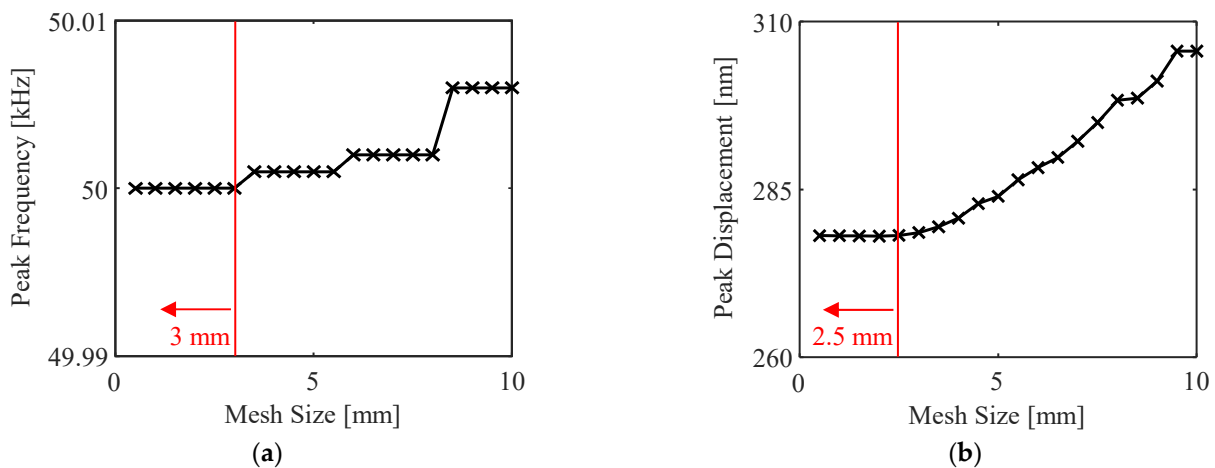


Figure 3. Mesh convergence test: Variations in (a) the peak frequency and (b) the corresponding peak displacement with respect to the mesh size that ranged from 0.5 mm to 10 mm in the time-harmonic analysis.

Figure 1b shows the configuration of the wave-propagation system that was used in the transient analysis. Figure 2 displays the workflow diagram used in COMSOL to perform the transient analysis. Wave-propagation analysis was performed using the ‘Time-dependent Study’ instead of the ‘Eigenfrequency Study’. PnC was constructed using the same procedure as the band-structure analysis described earlier, with an additional

structure attached to both ends with a length equal to twice the wavelength at the target frequency. The ‘Low Reflecting Boundary’ function within the ‘Solid Mechanics Physics’ was applied to both ends of the entire structure to implement semi-infinite conditions. In this case, the ‘Damping Type’ function was set to ‘P and S Waves’. An incident burst wave was generated as an initial condition in the middle of the attached structure on the left side using the ‘Prescribed Displacement’ function within the ‘Solid Mechanics Physics’. The mathematical expression for the incident waves of arbitrary cycle N is as follows.

$$u_{\text{In}}(t) = U_{\text{In}} \sin(2\pi f_t t) \times \left(H(t) - H\left(t - \frac{N}{f_t}\right) \right) \quad (1)$$

where the time variable t ranges from zero to 10 ms ($=500/f_t$), and the total time length is determined through trial and error. U_{In} represents the displacement amplitude of 10 nm, while f_t denotes the target frequency of 50 kHz. The Heaviside unit step functions $H(\cdot)$ were used in Equation (1) to limit the time range of wave excitation. Figure 4a shows one examples of the excited waveforms in terms of time when $n = 50$, while Figure 4b provides a closer view of these waveforms in the time domain from 0.9 ms to 1.1 ms. To ensure the stability and convergence of the results, the CFL (Courant–Friedrichs–Lewy) number was set to 0.2 [32–34], and the numerical time step was 116.19 ns. The default settings were used except for the parts mentioned earlier. The focus of this transient analysis was to quantitatively evaluate the performance of defect-mode-enabled energy localization. Here, the temporal displacement at the center of the defect was calculated.

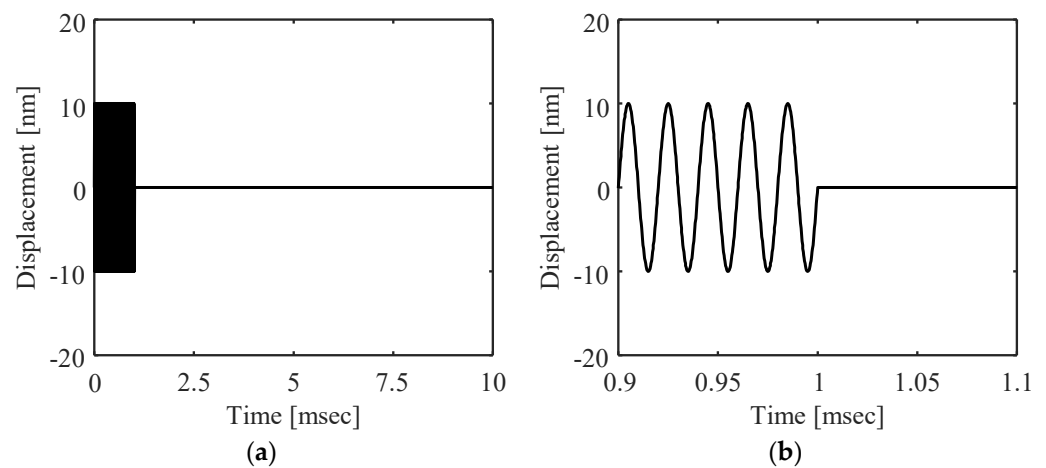


Figure 4. An example of excitation of burst waves when $n = 50$: (a) A time range from zero to 10 ms and (b) A time range from 0.9 ms to 1.1 ms.

3. Results and Discussion

In Figure 5a, the band-structure results of longitudinal waves are depicted, with the x -axis representing the normalized Bloch wavenumber ($=\text{Bloch wavenumber} \times \text{PnC Length}$) within the range of $[0, \pi]$ and the y -axis representing the frequency within the range of $[0 \text{ kHz}, 100 \text{ kHz}]$. The black and red solid lines depict the passband calculation results outside and inside the phononic band gap, respectively. The gray box marks the phononic band gap for longitudinal waves, spanning from 38.90 kHz to 61.10 kHz. Within the band gap, one defect band appears with a nearly zero slope from 49.97 kHz to 50.03 kHz. As suggested by Ref. [31], increasing the number of unit cells led to a flattened defect band, and its corresponding frequency range gradually converged to 50 kHz, which was obtained at the center of the Brillouin zone. Indeed, the enlarged view shown in Figure 5b supports this statement. Hence, this frequency can be considered the representative defect-band frequency. It can be confirmed that this defect-band frequency is also equal to the target frequency. Physically, the defect band had a group velocity of zero since the instantaneous slope of the band structure represented the group velocity (energy-transport velocity). This

means that the elastic wave energy could not be transferred through space, resulting in the energy being localized in the vicinity of the defect.

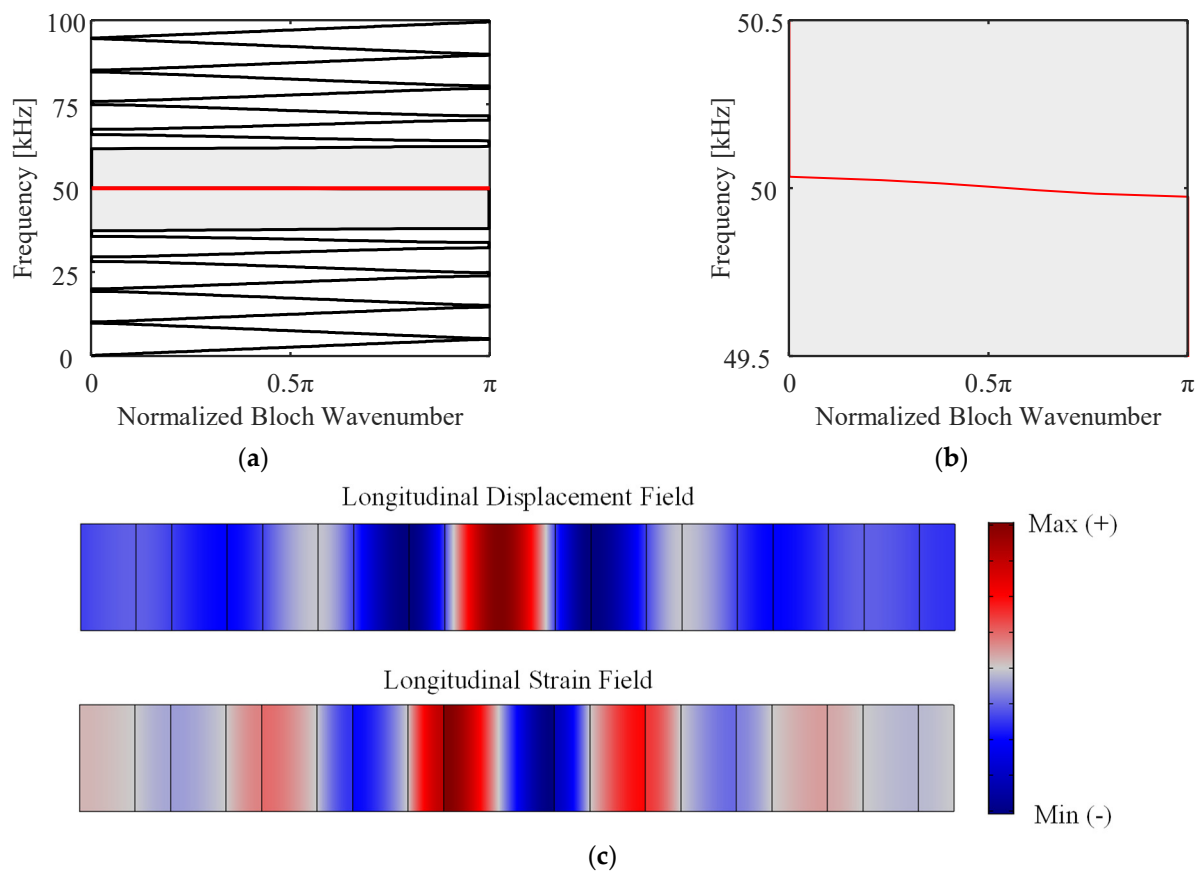


Figure 5. Results of the defect-band analysis: (a) Emergence of a phononic band gap ranging from 38.90 kHz to 61.10 kHz, (b) Emergence of one defect band range from 49.97 kHz to 50.03 kHz, and (c) Longitudinal displacement and strain field at the defect-band frequency of 50 kHz.

At the defect-band frequency of 50 kHz, Figure 5c shows the normalized longitudinal displacement and strain fields, respectively, of the defect-introduced PnC. It can be confirmed that this defect exhibited significantly enhanced behaviors at the defect-band frequency. It is noteworthy that the displacement field exhibited line symmetry with respect to the center of the defect, with the maximum displacement at the center of the defect, whereas the strain field featured point symmetry, with the maximum strain near the ends of the defect. Note that the displacement field is a continuous function, whereas the strain field is a discontinuous function at each boundary where the material varies. An analysis of the defect band could provide information on the frequency at which the elastic wave energy is localized and the shape in which this occurs.

Next, we needed to determine which physical quantity (e.g., displacement and strain) to examine at which point in the transient analysis. Referring to the previously discussed defect-mode shape, we aimed to investigate the longitudinal displacement at the center of the defect. When imagining the experiment, it would be easier to measure the displacement in a non-contact way using a Laser Doppler Vibrometer rather than measuring the strain by attaching a strain gauge to the defect [35–37]. One point worth mentioning before the analysis was the consideration of two reference values. First, the amplitude of the longitudinal displacement of the incident waves was equal to 10 nm, as mentioned in Equation (1). Second, the maximum longitudinal displacement amplitude at the frequency of 50 kHz in the time-harmonic analysis was 278 nm (ratio: 27.8); notably, this value corresponded to the peak value in the frequency response function of the longitudinal

displacement amplitude. This result can be understood in the same context as the value that converged with respect to the mesh size in Figure 3.

Figure 6 illustrates the calculated longitudinal displacement at the center of the defect for $n = 5, 15, 30, 50, 100, 200, 300, 500, 800,$ and 1000 cycles. The x -axis of all plots in Figure 6 stands for time, ranging from zero to 10 ms, and the y -axis stands for the longitudinal displacement, ranging from -350 nm to 350 nm. For a clear comparison among figures, Table 1 summarizes the times at which the maximum displacement could be achieved for each cycle, along with the corresponding positive displacement values. In addition, the end time when the excitation of burst waves was completed was also listed for each cycle. One thing to mention is that while the maximum amplitude was obtained at a time slightly greater than the time when the excitation ended in Figure 6a–g, the maximum displacement amplitude was obtained at the same time in Figure 6h–j. Additionally, it could be seen that the corresponding displacements had the same values. In fact, Figure 6h–j had similar plots. Several important observations are summarized as follows:

- (1) As the number of cycles increased, the time to reach the maximum displacement gradually increased and then converged to a certain value. Especially in the case of Figure 6i ($n = 800$) and j ($n = 1000$), the maximum displacement was obtained within the given time length of 10 ms even though the excited burst waves still entered the system after the max time of 8.56 ms. This suggested that the setup used to generate the burst waves could simulate time-harmonic analysis for a large number of cycles (here, $n > 500$).
- (2) Similar to the first observation, the maximum displacement also gradually increased and stabilized at the value obtained from time-harmonic analysis. This result could be interpreted in two ways. First, as the number of cycles increased, more cycles existed inside the defect introduced by PnC due to the occurrence of additional reflections and transmissions within the structure. Second, the phononic bandgap and defect-band characteristics were strengthened as the dynamic behavior approached a steady state.
- (3) The energy-localization performance of burst waves with a small number of cycles depended heavily on the number of cycles, even for the identically configured, defect-introduced PnCs. Taking into account the sensitivity of the burst wave setting, even in an ideal scenario (the semi-infinite condition and monochromatic wave), we concluded that comparing the energy-localization performance under incident waves with different cycle numbers for different systems might not be appropriate.
- (4) There was some improvement in the energy-localization performance of a small number of burst waves; however, this was still small compared to the cases of time-harmonic analysis or burst waves with a large number of cycles. Although we could not say that there were no defect modes, the fixed-like boundary condition was not clearly generated by the band gap. Therefore, it is appropriate to state that the defect-mode-based energy localization was not clear in this case of a small number of burst waves.

To supplement the discussions regarding the third and fourth investigations, Figure 7a–c superimposes the displacement fields obtained over time from the longitudinal centerline of the defect for $n = 5, 30,$ and 1000, respectively. As a comparative study, Figure 7d shows the displacement fields with various temporal phases in the time-harmonic analysis. The x -axis represents the designated space that denotes the two ends of the defect. The different displacement fields calculated a series of times before and after the maximum time in Table 1 are plotted simultaneously. One thing to focus on is the temporal evolution of the displacement at the left end. Referring to previous work in [31], this target-frequency-customized, defect-introduced PnC should manifest the nodal point (exactly zero values of longitudinal displacement) at each end of the defect, and a perfect standing wave pattern could be observed inside the defect at the frequency of the defect band. From this perspective, Figure 7c presents the zero-valued displacements at both ends, similar to Figure 7d. In contrast, it could be seen in Figure 7a,b that the displacement value at the left end fluctuated with the basis of a zero value. Hence, for burst waves with a small number

of cycles, it was difficult to consider the group velocity as practically zero because the nodal points possessed fluctuating characteristics over time. On the other hand, burst waves with a large number of cycles had a group velocity almost close to zero, such as in continuous wave situations.

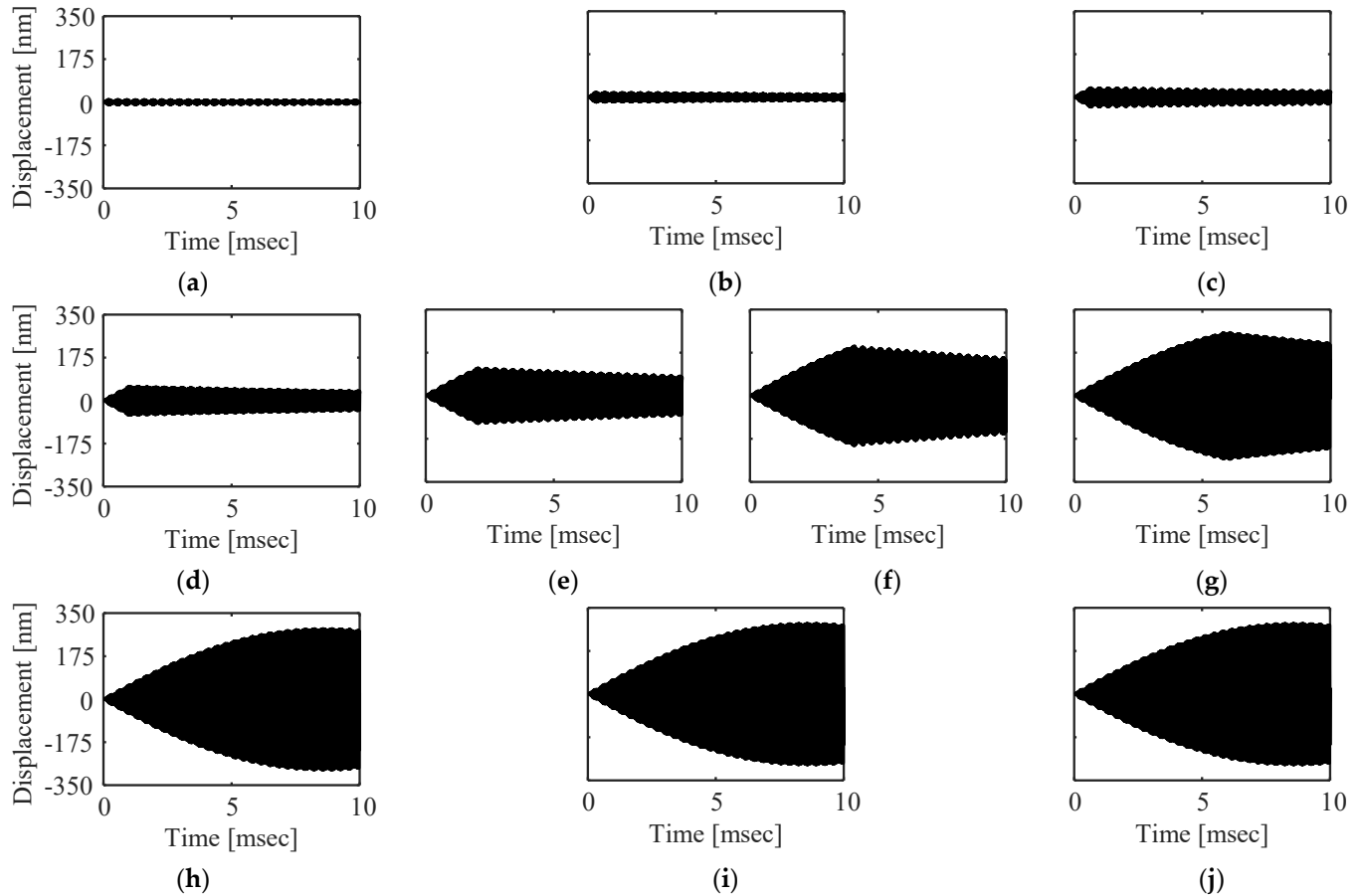


Figure 6. Results of the transient analysis: (a) $n = 5$, (b) $n = 15$, (c) $n = 30$, (d) $n = 50$, (e) $n = 100$, (f) $n = 200$, (g) $n = 300$, (h) $n = 500$, (i) $n = 800$, and (j) $n = 1000$.

Table 1. The times at which the maximum displacement was achieved for each cycle along with the corresponding displacement values.

Number of Cycles	5	15	30	50	100	200	300	500	800	1000
Max Displacement [nm]	11	20	39	58	113	202	257	287	287	287
Max Time [ms]	0.18	0.32	0.64	1.02	2.04	4.04	6.08	8.56	8.56	8.56
End Time [ms]	0.1	0.3	0.6	1	2	4	6	10	16	20

As mentioned in the Introduction, one question posed is whether it is valid to compare which defect-introduced PnC design achieved higher energy-localized behaviors under different input cycle conditions for different systems. The other question raised includes whether it is reasonable to claim that fewer cycles of burst waves achieved defect-mode-enabled energy localization from the viewpoint of resonance and band-gap formations. In order to provide a solution to these questions, the trend of energy-localization performance was analyzed across multiple scenarios of cycles rather than focusing on specific cycle numbers of burst waves or continuous waves. Figures 6 and 7 distinctly differentiate this research from previous work. This study suggests that (i) the preferred way to make a fair comparison and evaluate the inherent energy-localization performance among two

or several different PnCs was to utilize continuous waves that could make the steady state of the systems or excite burst waves with a sufficient number of cycles and (ii) clear the physically reasonable formation of defect-mode-enabled energy localization required from burst waves with a large number of cycles. Note that the required number of cycles varied with the system settings (e.g., geometric dimensions [38], material properties [39], the number of unit cells, and defect location [40]), and the damping effects are shown in Appendix A.

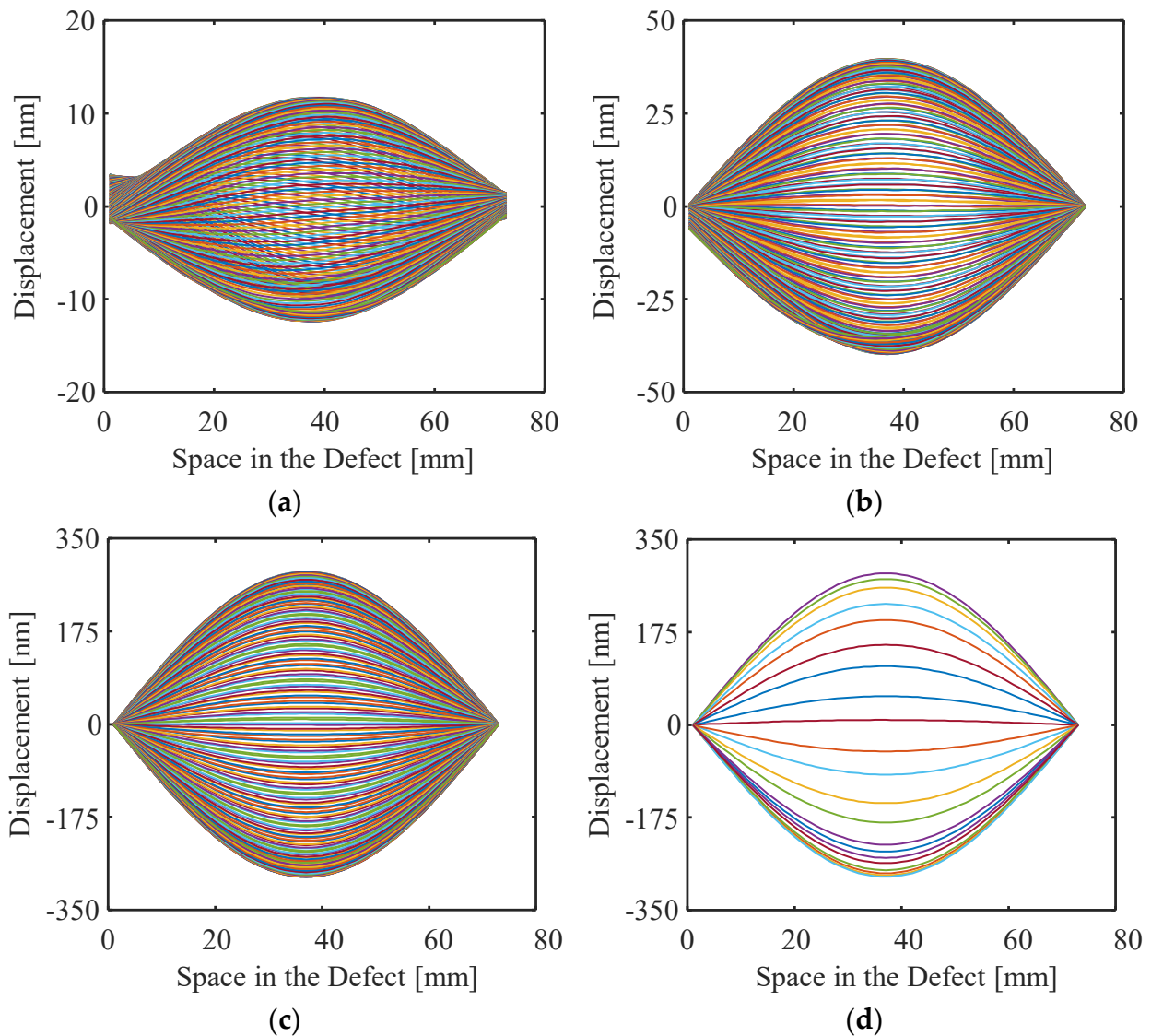


Figure 7. The overlaps of the displacement fields calculated over time within the defect: (a) $n = 5$, (b) $n = 30$, (c) $n = 1000$ in the transient analysis, and (d) Time-harmonic analysis.

4. Conclusions

This study investigated the energy-localization performance of one-dimensional phononic crystals (PnCs) with defects exposed to longitudinal, burst waves of different cycle numbers at the same defect-band frequency. A finite element method was used in a numerical case study to perform band-structure and transient analyses. The band-structure analysis identified the phononic band-gap range, one defect-band frequency, and the corresponding displacement/strain fields. The transient analysis quantified how much an incident burst wave was amplified over time within a defect for various cycle scenarios. The important observations were summarized as follows: (1) More cycles increased the time to reach the maximum displacement but converged after a point; here,

more than 500 cycles simulated time-harmonic analysis. (2) The maximum displacement stabilized at the time-harmonic value due to additional reflection/transmission within the defect-introduced PnC or phononic bandgap strengthening. (3) The energy localization of burst waves with a small cycle depended heavily on the cycle number; hence, comparing the energy-localization performance for different systems with different cycle numbers was inappropriate. (4) The energy-localization performance improved for burst waves with a small cycle but not as much as time-harmonic or burst waves with a large cycle (in this study, over 500). Therefore, the small number of cycles had difficulty presenting the physically meaningful defect-mode-enabled localization. Thus, this study recommended using continuous waves or burst waves with a sufficient number of cycles to evaluate the inherent energy-localization performance among two or several different PnCs, in order to make a fair comparison.

One may throw a question of whether the observations and messages revealed in this study could be generalized. Before thinking of defect-mode-enabled energy localization, it is necessary to consider the universal characteristics of phononic band gaps. A phononic band gap results from the destructive interferences that occur due to the continuously repeated generation of reflection and transmission throughout PnCs. It is well known that even in the case of continuous waves if the number of unit cells is insufficient or the impedance contrast is small, the band-gap performance becomes weak. Suppose we applied this investigation to a burst wave situation (keeping the number of unit cells and impedance contrast constant). In that case, a smaller number of cycles would mean a lower generation of transmission and reflection. Therefore, it can be reasonably speculated that the band-gap performance generally weakened. In this context, the weakening of band-gap performance could be generalized as a reduction in the defect-mode-enabled energy-localization performance [10]. Similarly, even in the case of continuous waves, fewer unit cells near the defect interrupt energy-localized behaviors [40]. Analogous to the temporal displacement at the resonance frequency relying on the mass and stiffness of the mass-spring system in vibrations, the cycle number at which the system reached a steady state varied depending on the configuration and specification of PnCs. Therefore, it was difficult to generalize the appropriate cycle number (in this case study, 500 cycles) for mimicking the time-harmonic analysis. However, phenomenally observed observations could be seen as general tendencies.

Funding: This work was supported in part by the Basic Science Research Program through the National Research Foundation of Korea (NRF), funded by the Ministry of Education under Grant 2022R1I1A1A01056406 and in part by the Dongguk University Research Fund of 2023.

Data Availability Statement: Not applicable.

Conflicts of Interest: The authors declare no conflict of interest.

Appendix A. Damping Effects on Energy-Localization Performance in Transient Analysis

This appendix discusses the variations in energy-localization performance due to damping effects [41–43]. In the transient analysis, Rayleigh damping should be considered if the materials used represent viscoelastic characteristics. The mathematic expression of Rayleigh damping is $\alpha[M] + \beta[K]$, where $[M]$ and $[K]$ denote the mass and stiffness matrices, respectively. The values considered for α and β are $(\alpha, \beta) = (0.00001 \times 10^5, 0.00001/10^5)$, $(0.00002 \times 10^5, 0.00002/10^5)$, $(0.00003 \times 10^5, 0.00003/10^5)$, and $(0.00004 \times 10^5, 0.00004/10^5)$. Figure A1 presents the displacement over time at the center of the defect for all cases when burst waves with 1000 cycles are excited. Each case corresponds to the plots colored with black, red, green, and blue. As the damping effects increased, it could be observed that the amount of displacement increasing over time decelerated, and the decreased level of localized energy localization led to a decrease in the displacements after a specific time. In the case of typical metals, the damping effects could be negligible, but in-depth research on viscoelastic materials appears to be necessary in the future.

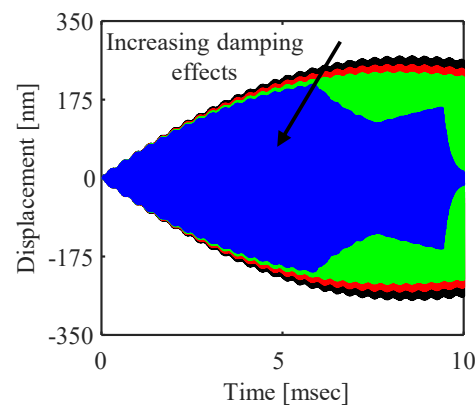


Figure A1. Damping effects on the displacement over time at the center of the defect for four cases when burst waves with 1000 cycles excited: $(\alpha, \beta) = (0.00001 \times 10^5, 0.00001/10^5)$ (black), $(0.00002 \times 10^5, 0.00002/10^5)$ (red), $(0.00003 \times 10^5, 0.00003/10^5)$ (green), and $(0.00004 \times 10^5, 0.00004/10^5)$ (blue).

References

1. Cang, Y.; Jin, Y.; Djafari-Rouhani, B.; Fytas, G. Fundamentals, progress and perspectives on high-frequency phononic crystals. *J. Phys. D Appl. Phys.* **2022**, *55*, 193002. [[CrossRef](#)]
2. Kennedy, J.; Lim, C. Machine learning and deep learning in phononic crystals and metamaterials: A review. *Mater. Today Commun.* **2022**, *33*, 104606.
3. Nomura, M.; Anufriev, R.; Zhang, Z.; Maire, J.; Guo, Y.; Yanagisawa, R.; Volz, S. Review of thermal transport in phononic crystals. *Mater. Today Phys.* **2022**, *22*, 100613. [[CrossRef](#)]
4. Lee, G.; Lee, D.; Park, J.; Jang, Y.; Kim, M.; Rho, J. Piezoelectric energy harvesting using mechanical metamaterials and phononic crystals. *Commun. Phys.* **2022**, *5*, 94. [[CrossRef](#)]
5. Oudich, M.; Gerard, N.J.; Deng, Y.; Jing, Y. Tailoring structure-borne sound through bandgap engineering in phononic crystals and metamaterials: A comprehensive Review. *Adv. Funct. Mater.* **2023**, *33*, 2206309. [[CrossRef](#)]
6. Jin, Y.; Jia, X.-Y.; Wu, Q.-Q.; He, X.; Yu, G.-C.; Wu, L.-Z.; Luo, B. Design of vibration isolators by using the Bragg scattering and local resonance band gaps in a layered honeycomb meta-structure. *J. Sound Vib.* **2022**, *521*, 116721. [[CrossRef](#)]
7. Pelat, A.; Gallot, T.; Gautier, F. On the control of the first Bragg band gap in periodic continuously corrugated beam for flexural vibration. *J. Sound Vib.* **2019**, *446*, 249–262. [[CrossRef](#)]
8. He, Z.; Zhang, G.; Chen, X.; Cong, Y.; Gu, S.; Hong, J. Elastic wave harvesting in piezoelectric-defect-introduced phononic crystal microplates. *Int. J. Mech. Sci.* **2023**, *239*, 107892. [[CrossRef](#)]
9. Lv, X.-F.; Fang, X.; Zhang, Z.-Q.; Huang, Z.-L.; Chuang, K.-C. Highly localized and efficient energy harvesting in a phononic crystal beam: Defect placement and experimental validation. *Crystals* **2019**, *9*, 391. [[CrossRef](#)]
10. Jo, S.-H.; Yoon, H.; Shin, Y.C.; Youn, B.D. Revealing defect-mode-enabled energy localization mechanisms of a one-dimensional phononic crystal. *Int. J. Mech. Sci.* **2022**, *215*, 106950. [[CrossRef](#)]
11. Geng, Q.; Wang, T.; Wu, L.; Li, Y. Defect coupling behavior and flexural wave energy harvesting of phononic crystal beams with double defects in thermal environments. *J. Phys. D Appl. Phys.* **2021**, *54*, 225501. [[CrossRef](#)]
12. Jo, S.-H.; Youn, B.D. A phononic crystal with differently configured double defects for broadband elastic wave energy localization and harvesting. *Crystals* **2021**, *11*, 643. [[CrossRef](#)]
13. Zhang, X.; Li, Y.; Wang, Y.; Jia, Z.; Luo, Y. Narrow-band filter design of phononic crystals with periodic point defects via topology optimization. *Int. J. Mech. Sci.* **2021**, *212*, 106829. [[CrossRef](#)]
14. Wu, L.-Y.; Wu, M.-L.; Chen, L.-W. The narrow pass band filter of tunable 1D phononic crystals with a dielectric elastomer layer. *Smart Mater. Struct.* **2008**, *18*, 015011. [[CrossRef](#)]
15. Zhong, J.; Xiang, J. Designing a phononic crystal with a large defect to enhance elastic wave energy localization and harvesting. *Jpn. J. Appl. Phys.* **2022**, *61*, 017002.
16. Hosseinkhani, A.; Ebrahimian, F.; Younesian, D.; Moayedizadeh, A. Defected meta-lattice structures for the enhanced localized vibrational energy harvesting. *Nano Energy* **2022**, *100*, 107488. [[CrossRef](#)]
17. Aly, A.H.; Nagaty, A.; Mehaney, A. One-dimensional phononic crystals that incorporate a defective piezoelectric/piezomagnetic as a new sensor. *Eur. Phys. J. B* **2018**, *91*, 211. [[CrossRef](#)]
18. Aly, A.H.; Mehaney, A. Phononic crystals with one-dimensional defect as sensor materials. *Indian J. Phys.* **2017**, *91*, 1021–1028. [[CrossRef](#)]
19. Jo, S.-H.; Lee, D.; Yoon, H.; Youn, B.D. Double piezoelectric defects in phononic crystals for ultrasonic transducers. *J. Phys. D Appl. Phys.* **2023**, *56*, 74002. [[CrossRef](#)]

20. Jo, S.-H.; Youn, B.D. Enhanced ultrasonic wave generation using energy-localized behaviors of phononic crystals. *Int. J. Mech. Sci.* **2022**, *228*, 107483. [[CrossRef](#)]
21. Park, C.-S.; Shin, Y.C.; Jo, S.-H.; Yoon, H.; Choi, W.; Youn, B.D.; Kim, M. Two-dimensional octagonal phononic crystals for highly dense piezoelectric energy harvesting. *Nano Energy* **2019**, *57*, 327–337. [[CrossRef](#)]
22. Fang, X.; Chuang, K.-C.; Yuan, Z.-W.; Huang, Z.-L. Defect mode-induced unidirectional flexural wave transmission using prismatic beams with concentrated gradient masses. *J. Appl. Phys.* **2018**, *123*, 224901. [[CrossRef](#)]
23. Thomes, R.L.; Beli, D.; Junior, C.D.M. Space–time wave localization in electromechanical metamaterial beams with programmable defects. *Mech. Syst. Signal Process.* **2022**, *167*, 108550. [[CrossRef](#)]
24. Lee, T.-G.; Jo, S.-H.; Seung, H.M.; Kim, S.-W.; Kim, E.-J.; Youn, B.D.; Nahm, S.; Kim, M. Enhanced energy transfer and conversion for high performance phononic crystal-assisted elastic wave energy harvesting. *Nano Energy* **2020**, *78*, 105226. [[CrossRef](#)]
25. Chuang, K.-C.; Zhang, Z.-Q.; Wang, H.-X. Experimental study on slow flexural waves around the defect modes in a phononic crystal beam using fiber Bragg gratings. *Phys. Lett. A* **2016**, *380*, 3963–3969. [[CrossRef](#)]
26. Jo, S.-H.; Shin, Y.C.; Choi, W.; Yoon, H.; Youn, B.D.; Kim, M. Double defects-induced elastic wave coupling and energy localization in a phononic crystal. *Nano Converg.* **2021**, *8*, 27. [[CrossRef](#)] [[PubMed](#)]
27. Lv, H.; Tian, X.; Wang, M.Y.; Li, D. Vibration energy harvesting using a phononic crystal with point defect states. *Appl. Phys. Lett.* **2013**, *102*, 034103. [[CrossRef](#)]
28. Aly, A.H.; Nagaty, A.; Khalifa, Z.; Mehaney, A. The significance of temperature dependence on the piezoelectric energy harvesting by using a phononic crystal. *J. Appl. Phys.* **2018**, *123*, 185102. [[CrossRef](#)]
29. Lv, X.-F.; Xu, S.-F.; Huang, Z.-L.; Chuang, K.-C. A shape memory alloy-based tunable phononic crystal beam attached with concentrated masses. *Phys. Lett. A* **2020**, *384*, 126056. [[CrossRef](#)]
30. Zhang, L.; Tan, T.; Yu, Z.; Yan, Z. Topological imbalanced phononic crystal with semi-enclosed defect for high-performance acoustic energy confinement and harvesting. *Nano Energy* **2022**, *100*, 107472. [[CrossRef](#)]
31. Jo, S.-H.; Youn, B.D. Designing a phononic crystal with a defect for target frequency matching using an analytical approach. *Mech. Adv. Mater. Struct.* **2022**, *29*, 2454–2467. [[CrossRef](#)]
32. Noh, G.; Ham, S.; Bathe, K.-J. Performance of an implicit time integration scheme in the analysis of wave propagations. *Comput. Struct.* **2013**, *123*, 93–105. [[CrossRef](#)]
33. Lei, Q.; Sornette, D. Transport and localization of Elastic waves in Two-dimensional fractured media: Consequences on scattering attenuation. *J. Geophys. Res. Solid Earth* **2021**, *126*, e2020JB021178. [[CrossRef](#)]
34. Kato, C.; Yamade, Y.; Wang, H.; Guo, Y.; Miyazawa, M.; Takaishi, T.; Yoshimura, S.; Takano, Y. Numerical prediction of sound generated from flows with a low Mach number. *Comput. Fluids* **2007**, *36*, 53–68. [[CrossRef](#)]
35. Park, H.W.; Seung, H.M.; Choi, W.; Kim, M.; Oh, J.H. Highly tunable low frequency metamaterial cavity for vibration localization. *Sci. Rep.* **2022**, *12*, 9714. [[CrossRef](#)]
36. Yoon, J.Y.; Lim, S.; Yoo, J.; Park, N.-C. Vibration reduction of cables with pendulum-type elastic metamaterials. *Int. J. Mech. Sci.* **2022**, *220*, 107169. [[CrossRef](#)]
37. Kim, D.-S.; Choi, W.; Kim, S.-W.; Kim, E.-J.; Nahm, S.; Kim, M. Correlating multimode strain and electrode configurations for high-performance gradient-index phononic crystal-based piezoelectric energy harvesting. *Mater. Horiz.* **2023**, *10*, 149–159. [[CrossRef](#)]
38. Wu, F.; Liu, Z.; Liu, Y. Splitting and tuning characteristics of the point defect modes in two-dimensional phononic crystals. *Phys. Rev. E* **2004**, *69*, 066609. [[CrossRef](#)]
39. Mehaney, A.; Ahmed, A.M. Modeling of phononic crystal cavity for sensing different biodiesel fuels with high sensitivity. *Mater. Chem. Phys.* **2021**, *257*, 123774. [[CrossRef](#)]
40. Jo, S.-H.; Yoon, H.; Shin, Y.C.; Choi, W.; Park, C.-S.; Kim, M.; Youn, B.D. Designing a phononic crystal with a defect for energy localization and harvesting: Supercell size and defect location. *Int. J. Mech. Sci.* **2020**, *179*, 105670. [[CrossRef](#)]
41. Frazier, M.J.; Hussein, M.I. Viscous-to-viscoelastic transition in phononic crystal and metamaterial band structures. *J. Acoust. Soc. Am.* **2015**, *138*, 3169–3180. [[CrossRef](#)] [[PubMed](#)]
42. Lucklum, R.; Mukhin, N. Enhanced sensitivity of resonant liquid sensors by phononic crystals. *J. Appl. Phys.* **2021**, *130*, 024508. [[CrossRef](#)]
43. Teymouri, S.; Ahmadi, H.; Rostami, A.; Matloub, S. Phononic crystal locally-resonant cavity for sensing metallic oxides nano-powders. *Int. J. Mech. Sci.* **2021**, *207*, 106658. [[CrossRef](#)]

Disclaimer/Publisher’s Note: The statements, opinions and data contained in all publications are solely those of the individual author(s) and contributor(s) and not of MDPI and/or the editor(s). MDPI and/or the editor(s) disclaim responsibility for any injury to people or property resulting from any ideas, methods, instructions or products referred to in the content.